

# FS-MedSAM2: Exploring the Potential of SAM2 for Few-Shot Medical Image Segmentation without Fine-tuning

Yunhao Bai<sup>1\*</sup>, Qinji Yu<sup>2,3\*</sup>, Boxiang Yun<sup>1</sup>, Dakai Jin<sup>3</sup>, Yingda Xia<sup>3</sup>, and Yan Wang<sup>1(✉)</sup>

<sup>1</sup> Shanghai Key Laboratory of Multidimensional Information Processing,  
East China Normal University  
{yhbai@stu.ecnu.edu.cn; ywang@ceee.ecnu.edu.cn}  
<sup>2</sup> Shanghai Jiao Tong University, Shanghai, China  
<sup>3</sup> DAMO Academy, Alibaba Group.

**Abstract.** The Segment Anything Model 2 (SAM2) has recently demonstrated exceptional performance in zero-shot prompt segmentation for natural images and videos. However, it faces significant challenges when applied to medical images. Since its release, many attempts have been made to adapt SAM2’s segmentation capabilities to the medical imaging domain. These efforts typically involve using a substantial amount of labeled data to fine-tune the model’s weights. In this paper, we explore SAM2 from a different perspective via making the full use of its trained memory attention module and its ability of processing mask prompts. We introduce FS-MedSAM2, a simple yet effective framework that enables SAM2 to achieve superior medical image segmentation in a few-shot setting, without the need for fine-tuning. Our framework outperforms the current state-of-the-arts on two publicly available medical image datasets. The code is available at [https://github.com/DeepMed-Lab-ECNU/FS\\_MedSAM2](https://github.com/DeepMed-Lab-ECNU/FS_MedSAM2).

## 1 Introduction

The Segment Anything Model 2 (SAM2) [13] has shown remarkable zero-shot prompt segmentation capabilities in natural images and videos. With a simple point or box as a prompt, SAM2 can accurately segment the object foreground within an image and track the object across frames in a video. However, similar to its predecessor, SAM [7], SAM2 struggles with medical images, particularly in Computed Tomography (CT) and Magnetic Resonance Imaging (MRI) scans. This limitation stems from the lack of medical images in its training data, resulting in the model’s inability to precisely delineate the boundaries of organs, tumors, and other structures in medical images, often leading to over-segmentation.

Recent studies [10,19,1] have sought to adapt SAM2 for medical imaging applications. Like fine-tuning on SAM, these approaches typically involve fine-tuning some components of SAM2, such as the mask decoder, using a certain

---

\* Equal contribution.

amount of labeled data. However, these methods face two primary limitations: first, they require a substantial amount of labeled data and considerable time for training; second, even after training, they still depend on interactive prompts to perform segmentation on the target images. Moreover, only taking cues from SAM, these methods inevitably overlook the fact that compared with SAM, SAM2 has made meaningful enhancements in its network architecture, resulting in a more capable and versatile successor. Though SAM2 struggles with directly segmenting medical images, it has the ability to attend to the previous memories of the target object via equipping with a memory attention module. This inspires us to explore it from a different perspective, *i.e.*, is it possible to leverage SAM2’s ability to segment targets based on similar images and their prompts in medical images, even without fine-tuning?

Few-shot medical image segmentation (FSMIS) aims to segment corresponding semantic regions in a query image using only a minimal number of support images and their associated segmentation masks. Most FSMIS methods treat consecutive slices from a volume as separate entities and segment each slice individually using the support images, which overlooks the shared semantic information across consecutive slices within the volume. Thanks to SAM2, which is equipped with two inherent advantages: (1) a well-trained memory attention module, attending to the previous memories of the target object, and (2) capable of processing mask prompts, corresponding to the few-shot input, leveraging SAM2 in FSMIS is intuitive but has not yet drawn any attention. Note that for the second advantage just mentioned, only mask prompt can yield good results, since point or box prompts cannot give precise boundary like nature images. To this end, we propose a framework within FSMIS that leverages SAM2’s video segmentation capabilities, utilizing the semantic information from slices adjacent to the query image to enhance segmentation accuracy.

In this paper, we propose FS-MedSAM2: a SAM2-based few-shot framework for medical image segmentation that requires no fine-tuning. Compared to fine-tuning on large labeled datasets, the few-shot scenario is more practical for medical segmentation tasks, considering certain rare diseases or working with unseen classes. Given 2D support images and their corresponding segmentation masks, our framework can segment the query images without the need for additional prompts. Furthermore, by incorporating semantic information from adjacent slices within the query volume, we can further improve segmentation performance. We validate FS-MedSAM2 on two publicly available datasets, CHAOS-MRI [6] and Synapse-CT [8], demonstrating its effectiveness by achieving state-of-the-art (SOTA) performance on both datasets.

## 2 Related Work

### 2.1 Segment Anything Model 2

Compared to SAM, which focuses solely on promptable image segmentation, SAM2 introduces an additional capability for promptable video segmentation. The components responsible for image segmentation in SAM2 remain the same

as those in SAM: the image encoder, prompt encoder, and mask decoder. In SAM2, the image encoder and prompt encoder independently encode the input image and prompt information, which are then fused and passed into the mask decoder to generate the segmentation mask.

For video segmentation, SAM2 incorporates additional components: the memory encoder, memory bank, and memory attention. The workflow can be summarized as follows:

1. **Add Prompt:** Initially, prompts are applied to select frames within the video (referred to as conditional frames). These frames undergo the standard image segmentation process independently, resulting in corresponding segmentation masks.
2. **Fill Memory Bank:** The image features and their associated masks are encoded by the memory encoder and stored in the memory bank.
3. **Propagate:** For frames without prompts (non-conditional frames), the image features are extracted by the image encoder and processed with memory attention using the information stored in the memory bank. After generating the mask for a frame, step 2 is repeated.

## 2.2 Adapt SAM2 to Medical Imaging

Similar to SAM, SAM2 also performs suboptimally on medical images when using point and box prompts. After SAM2 was released, several studies built upon the successful adaptations of SAM for medical imaging, aiming to adapt SAM2 for the medical image domain. For example, MedicalSAM2 [19] and MedSAM [10] fine-tune the mask decoder, while SAM2-Adapter [1] introduces lightweight adapters into the image encoder, which are fine-tuned alongside the mask decoder during weight updates.

In the SAM2 architecture, the image encoder is significantly more complex than the mask decoder. The success of these approaches, which primarily focus on fine-tuning the mask decoder, suggests that SAM2’s image encoder is already capable of effectively encoding the information present in medical images. In contrast to these methods, our approach aims to adapt SAM2 to medical imaging in a more challenging setting: few-shot learning without any weight fine-tuning.

## 2.3 Few-Shot Medical Image Segmentation

Few-shot medical image segmentation (FSMIS) is an emerging field that addresses the challenge of limited annotated data—a common issue in the medical domain due to the high costs, complexity of annotation, and legal constraints on data sharing. FSMIS techniques can be broadly categorized into two main types: prototypical network-based models [12,5,15,18] and two-branch interaction-based models [14,4,16,3]. These methods train a model to segment the query image by drawing information from the support image and its mask, and then validate the model on unseen categories that are not part of the training process.

However, most of these methods treat consecutive slices as independent entities, segmenting each slice separately in a few-shot manner. We believe that in a sequence of consecutive slices, the segmentation results of earlier slices can be leveraged to assist in the segmentation of subsequent slices. To explore this, we design experiments involving both support and query volumes, where the slices in the query volume reference the segmentation results of previously segmented slices within the same volume. This approach further enhances segmentation performance.

### 3 Method

The workflow of FS-MedSAM2 is illustrated in Fig. 1. Given  $N$  support images  $\mathbf{X}_N^S = \{X_0^S, X_1^S, \dots, X_{N-1}^S\}$  and their corresponding segmentation masks (*i.e.*, support mask)  $\mathbf{Y}_N^S = \{Y_0^S, Y_1^S, \dots, Y_{N-1}^S\}$ , the memory encoder generates support memories by downsampling the support mask using a convolutional module and summing it element-wise with the support feature embeddings from the image-encoder. The encoded support memories are then stored in the memory bank for the following query segmentation. For the  $M$  query images, we sequentially feed each image in  $\mathbf{X}_M^Q = \{X_0^Q, X_1^Q, \dots, X_{M-1}^Q\}$  into the image encoder, and the output query image features are sent to the memory attention module to fuse the memories stored in the memory bank via cross-attention. Then the memory-conditioned features are fed into the mask decoder for segmentation predictions. With the predicted query masks, we can encode the query memories in the same way as encoding the support memories and update the memory bank with the new query memories. For the  $t$ -th image  $X_t^Q$  in  $\mathbf{X}_M^Q$ , its predicted mask  $P_t$  is obtained as follows:

$$P_t = \mathcal{F}_{\text{SAM2}}(X_t^Q \mid \mathbf{X}_N^S, \mathbf{Y}_N^S; \mathbf{X}_{t-1}^Q), \quad (1)$$

where  $\mathcal{F}_{\text{SAM2}}(\cdot)$  is the SAM2 model. Before processing the query image  $X_t^Q$ ,  $N$  support images and their corresponding masks, along with  $t-1$  query images  $\mathbf{X}_{t-1}^Q$ , have been fed into the SAM2 model, and their features have been stored in the memory bank.

A key aspect of our framework lies in the use of mask prompts. Previous work has primarily focused on using points and boxes as prompts, often overlooking the potential of mask prompts. While mask prompts are more costly to obtain than points or boxes, and their use might seem to diminish the need for segmentation, we have found them to be highly beneficial in SAM2.

Based on our observations, providing an accurate mask prompt allows SAM2 to clearly understand and delineate the expected boundaries within the image. This ensures that the information encoded in the memory bank is more accurate, providing a solid foundation for successfully identifying the corresponding object boundaries in the query image.

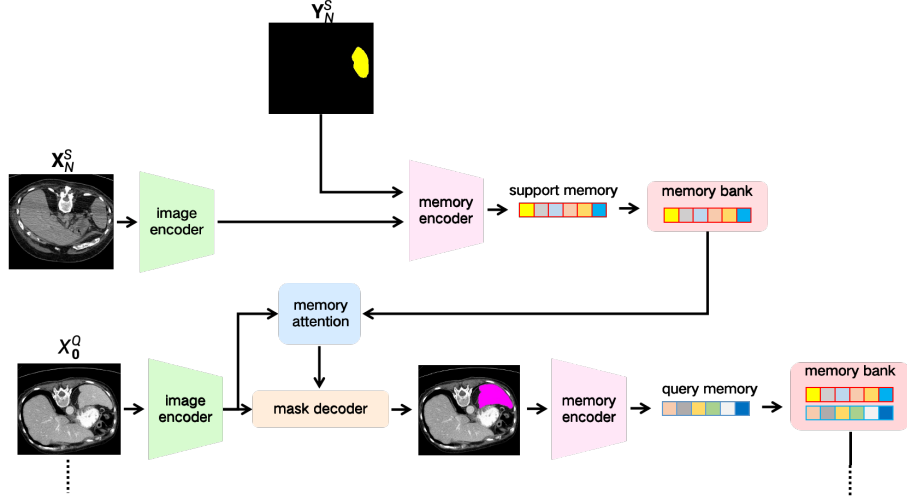


Fig. 1: Overall framework of FS-MedSAM2. The figure illustrates the framework when  $N = 1$ .

## 4 Experiments

### 4.1 Datasets

We validate FS-MedSAM2 on two widely-used public datasets.

(a) **Synapse-CT** [9] is an abdominal CT dataset acquired from the MICCAI 2015 Multi-Atlas Abdomen Labeling Challenge, which comprises 30 3D abdominal CT scans. Following GMRD [2], we evaluate FS-MedSAM2 on left kidney, right kidney, liver, and spleen.

(b) **CHAOS-MRI** [6] is an abdominal MRI dataset obtained from the ISBI 2019 Combined Healthy Abdominal Organ Segmentation Challenge. It contains 20 3D T2-SPIR MRI scans. Following GMRD [2], we also evaluate FS-MedSAM2 on the left kidney, right kidney, liver and spleen.

### 4.2 Implementation Details

**SAM2 Model** Unless otherwise specified, we use the SAM2 Hiera Tiny model by default for experiments. Comparative experiments with different sizes of SAM2 models are reported in the ablation study.

**Evaluation Metric** Following GMRD, we use the widely adopted metric Sorenson-Dice coefficient [11] in the FSMIS domain for evaluation, which is defined as:

$$DSC(P, Y) = \frac{2|P \cap Y|}{|P| + |Y|}, \quad (2)$$

where  $P$  and  $Y$  respectively represent the sets of foreground pixels in the predicted mask and the ground truth labels. Dice score falls between 0 and 1, indicating the similarity between the prediction and the ground truth.

### 4.3 Evaluation Details

Following GMRD, for evaluating new class segmentation, both the support volume  $\mathbf{X}^S$  and query volume  $\mathbf{X}^Q$  are divided into three positional sub-volumes: upper, middle, and lower, resulting in  $[\mathbf{X}_{N_{up}}^S, \mathbf{X}_{N_{mid}}^S, \mathbf{X}_{N_{low}}^S]$  and  $[\mathbf{X}_{M_{up}}^Q, \mathbf{X}_{M_{mid}}^Q, \mathbf{X}_{M_{low}}^Q]$ . From each support sub-volume, one slice is extracted to form the support set  $\mathbf{X}_3^S = \{X_0^S, X_1^S, X_2^S\}$ , where  $X_0^S \in \mathbf{X}_{M_{up}}^S$ ,  $X_1^S \in \mathbf{X}_{M_{mid}}^S$ , and  $X_2^S \in \mathbf{X}_{M_{low}}^S$ . The support image and its mask is then used to segment their corresponding query sub-volumes, *i.e.*,  $X_0^S$  and  $Y_0^S$  support the segmentation of  $\mathbf{X}_{M_{up}}^Q$ ,  $X_1^S$  and  $Y_1^S$  support the segmentation of  $\mathbf{X}_{M_{mid}}^Q$  and so on.

**Experimental Settings** We adopt a commonly-used One-Shot One-Query (1S1Q) setting, following prior arts [17,5,2]. Moreover, we propose a more resource-efficient setting, using only one support image in  $\mathbf{X}_N^S$ , where  $N = 1$ . In this setting, we design a Few-Query strategy, which incorporates the semantic information from neighboring slices. We term this resource-efficient setting with our designed strategy as Strictly One-Shot Few-Query (S1SFQ).

**One-Shot One-Query (1S1Q)** One-Shot One-Query refers to using one support image to infer the segmentation of one query image at a time, which is the inference method employed by previous works [17,5,2]. In our approach, for each query image  $X_i^Q$ , we perform the following inference steps to obtain the predicted mask  $P_i$ :

$$P_i = \mathcal{F}_{\text{SAM2}}( X_i^Q \mid X_j^S, Y_j^S; \text{None} ), \quad (3)$$

$$\text{where } j = \begin{cases} 0, & \text{if } X_i^Q \in \mathbf{X}_{M_{up}}^Q, \\ 1, & \text{if } X_i^Q \in \mathbf{X}_{M_{mid}}^Q, \\ 2, & \text{if } X_i^Q \in \mathbf{X}_{M_{low}}^Q. \end{cases} \quad (4)$$

In this scenario, each query image is segmented using only the support image and mask information stored in the memory bank, without leveraging the segmentation results of neighboring slices with similar semantics as auxiliary information. To address this issue, we designed an alternative validation approach that incorporates the semantic information from neighboring slices.

**Strictly One-Shot Few-Query (S1SFQ)** To utilize the results inferred from adjacent query slices to enrich the information in the memory bank, we process an entire query image set  $\mathbf{X}_M^Q$  as a whole during inference, where  $M = M_{up} +$

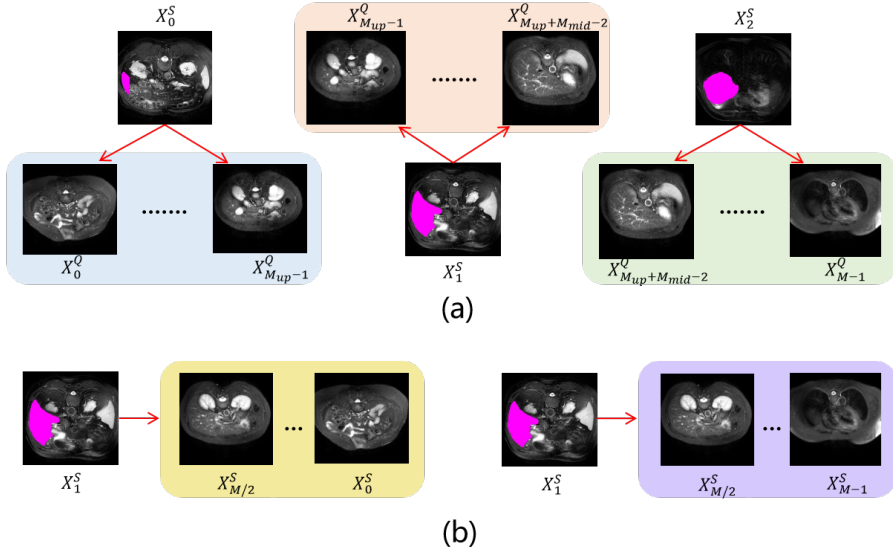


Fig. 2: Explanatory diagram for 1S1Q (a) and S1SFQ (b). In 1S1Q, each sub-query volume has a corresponding support image and its mask; in S1SFQ, only one support image is used for the entire query volume.

$M_{mid} + M_{low}$ . The query image set is stacked in the axial view, with  $X_0^Q$  and  $X_{M-1}^Q$  corresponding to the top and bottom slices of the segmented organ, where the foreground regions are usually very small.

When a query image set is processed sequentially during inference, the first image to be inferred is often the most challenging. This can lead to poor initial segmentation results, which may contaminate the memory bank and degrade the accuracy of subsequent inferences. To mitigate this issue, we split the query image set  $\mathbf{X}_M^Q$  into two parts:  $\dot{\mathbf{X}}_{M/2:0}^Q$  and  $\ddot{\mathbf{X}}_{M/2:M-1}^Q$ . The set  $\dot{\mathbf{X}}_{M/2:0}^Q = \{X_{M/2}^Q, X_{M/2-1}^Q, \dots, X_0^Q\}$  represents the slices from 0 to  $M/2$  stacked in descending order, while  $\ddot{\mathbf{X}}_{M/2:M-1}^Q$  represents the slices from  $M/2$  to  $M$  stacked in ascending order. This operation aims to prioritize the inference of easier slices (those with larger foreground regions) when processing the query image set, ensuring that the memory bank contains more accurate encoded information, which can improve the segmentation of subsequent slices.

To further validate that our framework remains effective even with a limited number of support images, we utilize a single support image  $X_1^S$  for the inference of the entire query volume  $\mathbf{X}^Q$ , rather than having a corresponding support image for each sub-volume like previous methods. We refer to this setting as “Strictly One-Shot”. Under this setting, the prediction  $P_i$  for  $X_i^Q$  is obtained as follows:

Dataset	Method	Spleen	Liver	LK	RK	Mean
Synapse-CT	AAS-DCL [ECCV' 22]	72.30	78.04	74.58	73.19	74.52
	RPT [MICCAI' 23]	79.13	<u>82.57</u>	77.05	72.58	77.83
	GMRD [TMI' 24]	78.31	79.60	81.70	74.46	78.52
	Ours(1S1Q)	<u>91.40</u>	81.04	<u>86.38</u>	<b>88.72</b>	<u>86.89</u>
	Ours(S1SFQ)	<b>93.95</b>	<b>85.89</b>	<b>93.02</b>	<u>83.49</u>	<b>89.09</b>
CHAOS-MRI	Q-Net [IntelliSys' 23]	75.99	81.74	78.36	87.98	81.02
	RPT [MICCAI' 23]	76.37	<u>82.86</u>	80.72	89.82	82.44
	GMRD [TMI' 24]	76.09	81.42	83.96	90.12	82.90
	Ours(1S1Q)	<u>87.80</u>	79.46	84.07	<u>91.97</u>	<u>85.83</u>
	Ours(S1SFQ)	<b>90.19</b>	<b>89.25</b>	<b>89.43</b>	<b>93.31</b>	<b>90.55</b>

Table 1: Quantitative comparisons (in Dice score %) with state-of-the-art FSMIS methods on Synapse-CT and CHAOS-MRI datasets. LK and RK denote left kidney and right kidney, respectively. The best performances are highlighted in **bold**, while the second-best performances are indicated with underlines.

$$P_i = \begin{cases} \mathcal{F}_{\text{SAM2}}( X_i^Q \mid X_1^S, Y_1^S; \dot{\mathbf{X}}_{M/2:i+1}^Q ), & \text{if } 0 \leq i < M/2, \\ \mathcal{F}_{\text{SAM2}}( X_i^Q \mid X_1^S, Y_1^S; \ddot{\mathbf{X}}_{M/2:i-1}^Q ), & \text{if } M/2 \leq i < M. \end{cases} \quad (5)$$

The explanatory diagram for 1S1Q and S1SFQ is shown in Fig. 2. We also conduct S1SFQ experiments without this operation, with detailed results presented in the ablation study.

#### 4.4 Comparison with SOTA Methods

To demonstrate the effectiveness and superiority of FS-MedSAM2, we select the three most competitive results on Synapse-CT and CHAOS-MRI for comparison [2]. For Synapse-CT, the methods compared are AAS-DCL [17], RPT [20], and GMRD. For CHAOS-MRI, the methods compared are Q-Net [15], RPT [20], and GMRD. The results are shown in Table 1.

As shown in the table, FS-MedSAM2 achieves the best performance on both datasets, with a significant margin of improvement. Notably, our framework demonstrates substantial improvements in spleen segmentation, a task where previous methods struggled. On the Synapse-CT dataset, we observe a 14.32% increase in the Dice score (93.95% vs. 79.13%), and on the CHAOS-MRI dataset, FS-MedSAM2 achieved a 13.82% increase (90.19% vs. 76.37%).

#### 4.5 Ablation Study

We conduct ablation studies on the size of support memory and the inference order of few-query to assess their impact on performance. Furthermore, we in-

Dataset	Support mem size	Model	Spleen	Liver	LK	RK	Mean
Synapse-CT	1S1Q	Tiny	<b>91.40</b>	81.04	86.38	<u>88.72</u>	86.89
		Small	89.55	<u>87.18</u>	86.29	86.89	87.48
		Base	89.08	<u>86.63</u>	86.14	<u>87.92</u>	87.44
		Large	79.66	<u>87.34</u>	<b>91.23</b>	82.82	85.26
	3S1Q	Tiny	<u>89.98</u>	<u>84.40</u>	87.45	<b>90.55</b>	<b>88.10</b>
		Small	86.28	<u>88.53</u>	87.21	85.87	86.97
		Base	88.58	<b>88.54</b>	87.97	86.69	<u>87.95</u>
		Large	80.17	87.73	<u>89.22</u>	88.33	86.36
CHAOS-MRI	1S1Q	Tiny	87.80	79.46	84.07	91.97	85.83
		Small	84.60	<b>92.50</b>	81.54	<u>93.35</u>	<u>88.00</u>
		Base	<b>91.27</b>	82.43	78.42	<b>93.55</b>	86.42
		Large	89.52	<u>87.59</u>	79.38	92.74	87.31
	3S1Q	Tiny	84.64	75.19	<b>88.89</b>	91.50	85.06
		Small	<u>90.88</u>	79.97	<u>86.03</u>	92.47	87.34
		Base	90.08	86.32	84.80	92.41	<b>88.40</b>
		Large	87.45	82.13	85.91	<u>93.35</u>	87.21

Table 2: Ablation study of support memory size in 1S1Q and 3S1Q (in Dice score %). The best performances are highlighted in **bold**, while the second-best performances are indicated with underlines.

vestigate the performance of different sizes of SAM2 models (Tiny, Small, Base and Large) under each setting.

**Size of Support Memory** Unlike in the 1S1Q setting where only one support image is used, we enrich the support memory by utilizing the entire  $\mathbf{X}_3^S$ , *i.e.*, the support memory contains the features of  $\mathbf{X}_3^S$ . Correspondingly, we refer to this setting as Three-Shot One-Query (3S1Q). This allows us to observe whether a more diverse support memory could improve performance. The inference step is:

$$P_i = \mathcal{F}_{\text{SAM2}}(X_i^Q \mid \mathbf{X}_3^S, \mathbf{Y}_3^S; \text{None}). \quad (6)$$

To more intuitively observe whether the size of the support memory affects segmentation performance, we summarize the results of the 3S1Q and 1S1Q settings in Table 2.

As shown in the table, when we treat each query image independently, the impact of the support memory size on performance is not significant. This is evident in the results, where increasing the support memory size from 1 to 3 does not consistently improve performance and may even lead to a decline in some cases. For instance, in CHAOS-MRI, SAM2 Tiny showed a 0.77% decrease in mean performance in the 3S1Q setting compared to the 1S1Q setting. At the same time, as the model size increases, there is no consistent trend of improvement in segmentation performance. Therefore, we recommend using the

Dataset	Inference order	Model	Spleen	Liver	LK	RK	Mean
Synapse-CT	From Top	Tiny	68.73	30.11	21.19	36.08	39.03
		Small	56.83	32.10	52.20	0.09	35.31
		Base	72.74	20.25	71.93	0.05	41.24
		Large	48.45	23.80	57.53	66.12	48.98
	From Middle	Tiny	93.95	85.89	93.02	83.49	89.09
		Small	90.43	88.80	93.35	83.21	88.95
		Base	94.99	88.01	94.85	84.20	90.51
		Large	89.79	89.08	84.32	82.20	86.35
CHAOS-MRI	From Top	Tiny	91.36	1.29	47.39	31.44	42.87
		Small	92.14	38.81	53.50	33.38	54.46
		Base	67.82	88.60	47.54	46.79	62.69
		Large	90.78	85.42	45.13	63.03	71.09
	From Middle	Tiny	90.19	89.25	89.43	93.31	90.55
		Small	89.31	84.87	87.55	93.44	88.79
		Base	88.29	86.32	87.04	93.66	88.83
		Large	88.34	88.59	75.30	93.69	86.48

Table 3: Ablation study of the inference order in S1SFQ (in Dice score %).

SAM2 Tiny model in a few-shot one-query setting, as it offers the smallest computational load and fastest processing speed while still delivering satisfactory performance.

**Inference Order of Few-Query** In S1SFQ, to avoid starting with the more challenging slices, we initiate the inference from the middle slice of the query volume. In this subsection, we conduct ablation experiments where inference begins from the top slice, which is formulated as:

$$P_i = \mathcal{F}_{\text{SAM2}}( X_i^Q \mid X_1^S, Y_1^S; \ddot{\mathbf{X}}_{0:i-1}^Q ). \quad (7)$$

As illustrated in Table 3 and Table 4, when we begin the inference process for the query volume from the top slice, the model’s segmentation performance experiences a significant decline. As described in the method section, when inference begins from the top slice of the query image set volume (which typically has the smallest organ foreground), it is less likely to accurately segment the foreground. This approach can lead to the inclusion of inaccurate mask information in the query memory, severely impacting the segmentation of subsequent slices. The same issue is observed in the 3S1Q setting as well.

However, in the S1SFQ setting, the size of the model shows a noticeable impact: as the model size increases, the segmentation performance improves. This may indicate that larger models are less dependent on query memory, as they can more effectively adaptively select useful information from both the support memory and query memory for segmentation. In contrast, smaller models

Dataset	Inference order	Model	Spleen	Liver	LK	RK	Mean
Synapse-CT	From Top	Tiny	74.01	49.31	85.79	74.54	70.91
		Small	43.04	44.54	58.48	61.51	51.89
		Base	89.55	35.33	72.39	38.29	58.89
		Large	59.29	54.38	61.03	86.54	65.31
	From Middle	Tiny	<u>95.33</u>	87.66	94.53	<u>92.01</u>	<u>92.38</u>
		Small	94.30	87.77	<u>94.69</u>	90.30	91.77
		Base	<b>95.35</b>	<u>89.21</u>	<b>95.12</b>	90.62	92.58
		Large	93.98	<b>90.48</b>	94.67	<b>92.13</b>	<b>92.82</b>
CHAOS-MRI	From Top	Tiny	<b>90.92</b>	89.96	84.06	77.57	85.63
		Small	90.47	76.55	47.29	77.76	73.02
		Base	90.14	<b>90.17</b>	67.69	91.17	84.79
		Large	88.73	89.24	72.91	87.19	84.52
	From Middle	Tiny	89.57	87.19	<b>91.99</b>	93.41	<u>90.54</u>
		Small	<u>90.57</u>	83.99	91.12	93.26	89.74
		Base	88.28	85.01	87.62	<u>93.58</u>	88.62
		Large	88.29	89.97	<u>91.70</u>	<b>93.70</b>	<b>90.92</b>

Table 4: Ablation study of the inference order in 3SFQ (in Dice score %).

tend to rely more heavily on query memory, making them more susceptible to inaccuracies in the query memory.

#### 4.6 Visualization

In Fig. 3 and Fig. 4, we present the segmentation visualization results of FS-MedSAM2 under the 1S1Q setting for the Synapse-CT and CHAOS-MRI datasets, respectively. For each class, we show each image in the support image set  $\mathbf{X}_3^S$  (Support) along with the corresponding example query prediction and ground truth.

The figures reveal an exciting phenomenon: even when there are significant differences between the foregrounds of the support image and the query image (such as size, position, and shape), our framework still manages to segment the object foreground effectively. This demonstrates that the object tracking capabilities of the SAM2 architecture are not limited to videos with minimal frame-to-frame differences. It also performs well on pairs of images with substantial variations.

## 5 Conclusion

In this paper, we introduce FS-MedSAM2, a new framework for applying SAM2 to medical images. This framework performs few-shot segmentation using mask prompts without any parameter fine-tuning and leverages SAM2’s video segmentation capabilities to utilize the semantic information from neighboring slices

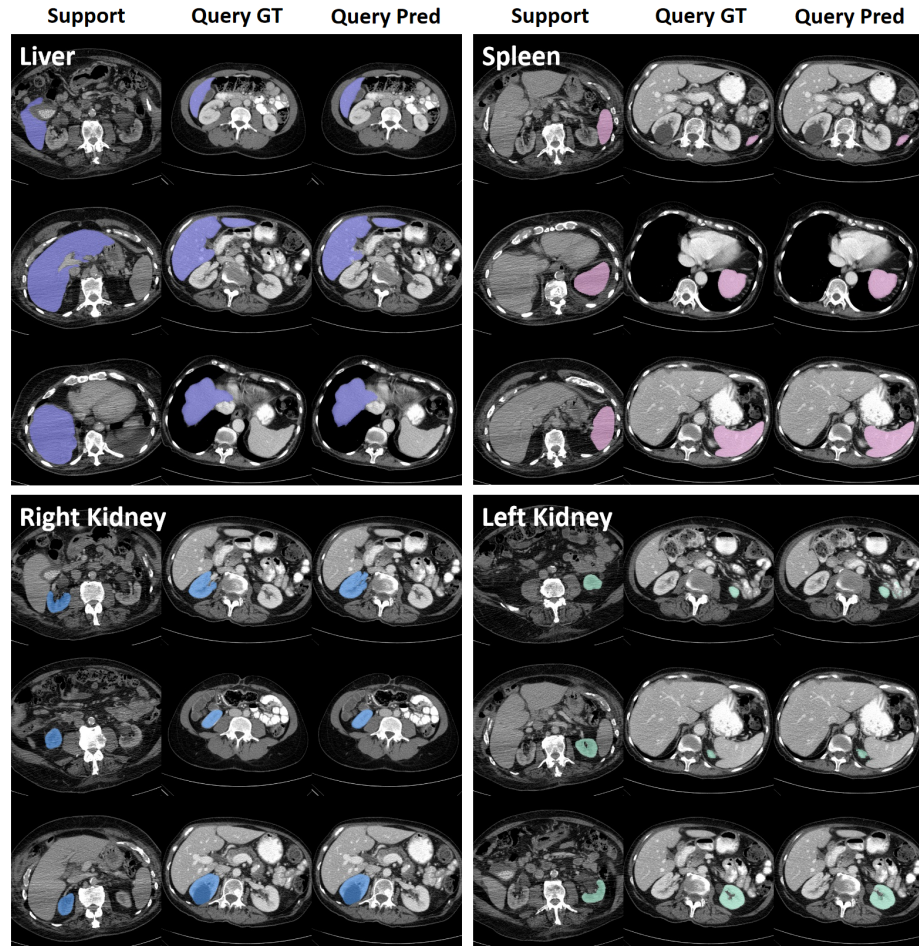


Fig. 3: Visualization results of Synapse-CT dataset.

within the query volume, achieving enhanced segmentation performance. Our framework demonstrated significant advantages on two publicly available medical datasets, proving the effectiveness of the approach. In future work, we will explore SAM2’s deeper capabilities in medical imaging and investigate more practical, real-world application scenarios.

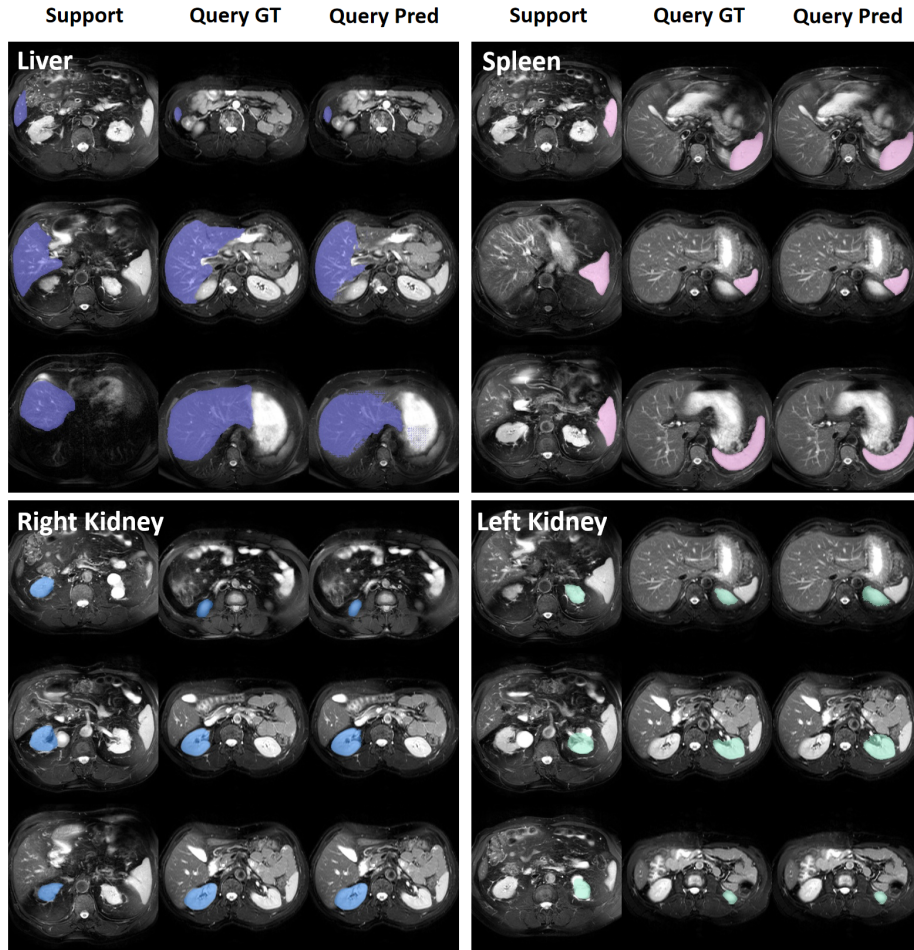


Fig. 4: Visualization results of CHAOS-MRI dataset.

## References

1. Chen, T., Lu, A., Zhu, L., Ding, C., Yu, C., Ji, D., Li, Z., Sun, L., Mao, P., Zang, Y.: Sam2-adapter: Evaluating & adapting segment anything 2 in downstream tasks: Camouflage, shadow, medical image segmentation, and more (2024), <https://arxiv.org/abs/2408.04579>
2. Cheng, Z., Wang, S., Xin, T., Zhou, T., Zhang, H., Shao, L.: Few-shot medical image segmentation via generating multiple representative descriptors. *IEEE Transactions on Medical Imaging* (2024)
3. Ding, H., Sun, C., Tang, H., Cai, D., Yan, Y.: Few-shot medical image segmentation with cycle-resemblance attention. In: *Proceedings of the IEEE/CVF Winter Conference on Applications of Computer Vision*. pp. 2488–2497 (2023)

4. Feng, R., Zheng, X., Gao, T., Chen, J., Wang, W., Chen, D.Z., Wu, J.: Interactive few-shot learning: Limited supervision, better medical image segmentation. *IEEE Transactions on Medical Imaging* **40**(10), 2575–2588 (2021)
5. Hansen, S., Gautam, S., Jenssen, R., Kampffmeyer, M.: Anomaly detection-inspired few-shot medical image segmentation through self-supervision with supervoxels. *Medical Image Analysis* **78**, 102385 (2022)
6. Kavur, A.E., Gezer, N.S., Bariş, M., Aslan, S., Conze, P.H., Groza, V., Pham, D.D., Chatterjee, S., Ernst, P., Özkan, S., et al.: Chaos challenge-combined (ct-mr) healthy abdominal organ segmentation. *Medical Image Analysis* **69**, 101950 (2021)
7. Kirillov, A., Mintun, E., Ravi, N., Mao, H., Rolland, C., Gustafson, L., Xiao, T., Whitehead, S., Berg, A.C., Lo, W.Y., Dollár, P., Girshick, R.: Segment anything. *arXiv:2304.02643* (2023)
8. Landman, B., Xu, Z., Igelsias, J., Styner, M., Langerak, T., Klein, A.: Miccai multi-atlas labeling beyond the cranial vault–workshop and challenge. In: Proc. MICCAI Multi-Atlas Labeling Beyond Cranial Vault—Workshop Challenge. vol. 5, p. 12 (2015)
9. Landman, B., Xu, Z., Igelsias, J., Styner, M., Langerak, T., Klein, A.: Miccai multi-atlas labeling beyond the cranial vault–workshop and challenge. In: Proc. MICCAI Multi-Atlas Labeling Beyond Cranial Vault—Workshop Challenge. vol. 5, p. 12 (2015)
10. Ma, J., Kim, S., Li, F., Baharoon, M., Asakereh, R., Lyu, H., Wang, B.: Segment anything in medical images and videos: Benchmark and deployment (2024), <https://arxiv.org/abs/2408.03322>
11. Ouyang, C., Biffi, C., Chen, C., Kart, T., Qiu, H., Rueckert, D.: Self-supervision with superpixels: Training few-shot medical image segmentation without annotation. In: Computer Vision–ECCV 2020: 16th European Conference, Glasgow, UK, August 23–28, 2020, Proceedings, Part XXIX 16. pp. 762–780. Springer (2020)
12. Ouyang, C., Biffi, C., Chen, C., Kart, T., Qiu, H., Rueckert, D.: Self-supervised learning for few-shot medical image segmentation. *IEEE Transactions on Medical Imaging* **41**(7), 1837–1848 (2022)
13. Ravi, N., Gabeur, V., Hu, Y.T., Hu, R., Ryali, C., Ma, T., Khedr, H., Rädle, R., Rolland, C., Gustafson, L., Mintun, E., Pan, J., Alwala, K.V., Carion, N., Wu, C.Y., Girshick, R., Dollár, P., Feichtenhofer, C.: Sam 2: Segment anything in images and videos (2024), <https://arxiv.org/abs/2408.00714>
14. Roy, A.G., Siddiqui, S., Pölsterl, S., Navab, N., Wachinger, C.: ‘squeeze & excite’-guided few-shot segmentation of volumetric images. *Medical image analysis* **59**, 101587 (2020)
15. Shen, Q., Li, Y., Jin, J., Liu, B.: Q-net: Query-informed few-shot medical image segmentation. In: Proceedings of SAI Intelligent Systems Conference. pp. 610–628. Springer (2023)
16. Sun, L., Li, C., Ding, X., Huang, Y., Chen, Z., Wang, G., Yu, Y., Paisley, J.: Few-shot medical image segmentation using a global correlation network with discriminative embedding. *Computers in biology and medicine* **140**, 105067 (2022)
17. Wu, H., Xiao, F., Liang, C.: Dual contrastive learning with anatomical auxiliary supervision for few-shot medical image segmentation. In: European Conference on Computer Vision. pp. 417–434. Springer (2022)
18. Yu, Q., Dang, K., Tajbakhsh, N., Terzopoulos, D., Ding, X.: A location-sensitive local prototype network for few-shot medical image segmentation. In: 2021 IEEE 18th international symposium on biomedical imaging (ISBI). pp. 262–266. IEEE (2021)

19. Zhu, J., Qi, Y., Wu, J.: Medical sam 2: Segment medical images as video via segment anything model 2 (2024), <https://arxiv.org/abs/2408.00874>
20. Zhu, Y., Wang, S., Xin, T., Zhang, H.: Few-shot medical image segmentation via a region-enhanced prototypical transformer. In: International Conference on Medical Image Computing and Computer-Assisted Intervention. pp. 271–280. Springer (2023)